Monthly Notices
of the
ROYAL ASTRONOMICAL SOCIETY

MNRAS **485,** 102–116 (2019)
Advance Access publication 2019 January 24

doi:10.1093/mnras/stz265

The 3D shape of Type IIb SN 2011hs

H. F. Stevance ,[1]★ J. R. Maund ,[1]† D. Baade,[2] J. Bruten,[1] A. Cikota ,[3] P. Höflich,[4] L. Wang,[5] J. C. Wheeler ,[6] A. Clocchiatti,[7] J. Spyromilio,[2] F. Patat,[2] Y. Yang[8] and P. Crowther[1]

[1]*Department of Physics and Astronomy, University of Sheffield, Hounsfield Rd, Sheffield S3 7RH, UK*
[2]*European Organisation for Astronomical Research in the Southern Hemisphere (ESO), Karl-Schwarzschild-Str. 2, D-85748 Garching b. München, Germany*
[3]*Physics Division, Lawrence Berkeley National Laboratory, 1 Cyclotron Road, Berkeley, CA 94720, USA*
[4]*Department of Physics, Florida State University, Tallahassee, FL 32306-4350, USA*
[5]*George P. and Cynthia Woods Mitchell Institute for Fundamental Physics and Astronomy, Texas A&M University*
[6]*Department of Astronomy and McDonald Observatory, The University of Texas at Austin, Austin, TX 78712, USA*
[7]*Institute of Astrophysics, Universidad Católica de Chile, and Millennium Institute of Astrophysics, Santiago, Chile*
[8]*Department of Particle Physics and Astrophysics, Weizmann Institute of Science, Rehovot 76100, Israel*

Accepted 2019 January 22. Received 2019 January 18; in original form 2018 December 20

ABSTRACT

We observed seven epochs of spectropolarimetry in optical wavelengths for the Type IIb SN 2011hs, ranging from −3 to +40 d with respect to *V*-band maximum. A high degree of interstellar polarization was detected (up to ∼3 per cent), with a peak lying blueward of 4500 Å. Similar behaviours have been seen in some Type Ia supernovae (SNe), but had never been observed in a Type IIb. We find that it is most likely the result of a relative enhancement of small silicate grains in the vicinity of the SN. Significant intrinsic continuum polarization was recovered at −3 and +2 d ($p = 0.55 \pm 0.12$ per cent and 0.75 ± 0.11 per cent, respectively). We discuss the change of the polarization angle across spectral lines and in the continuum as diagnostics for the 3D structure of the ejecta. We see a gradual rotation by about −50° in the continuum polarization angle between −2 and +18 d after *V*-band maximum. A similar rotation in He I λ5876, Hα and the Ca II infrared triplet seems to indicate a strong influence of the global geometry on the line polarization features. The differences in the evolution of their respective loops on the Stokes $q - u$ plane suggest that line specific geometries are also being probed. Possible interpretations are discussed and placed in the context of literature. We find that the spectropolarimetry of SN 2011hs is most similar to that of SN 2011dh, albeit with notable differences.

Key words: techniques: polarimetric – supernovae: general – supernovae: individual: SN 2011hs.

1 INTRODUCTION

At the end of their lives, the cores of massive stars ($M_{ZAMS} > 8\ M_\odot$) collapse, which can result in core-collapse supernovae (CCSNe). There are multiple types of CCSNe: Type II SNe show strong hydrogen features in their spectra, whereas Type Ib/c SNe do not. Type Ib and Ic SNe are differentiated based on the presence (Ib) or absence (Ic) of helium in their spectra. There also exists a transitional type of SN that bridges the gap between Type II and Type Ib SNe: the Type IIb, whose spectrum evolves from being hydrogen dominated (Type II) to being helium dominated (Ib – Filippenko 1997; Branch & Wheeler 2017). Type IIb SNe arise from progenitors that have been stripped of nearly all of their hydrogen envelope, retaining less than 0.5 $M_\odot$ (Smith et al. 2011). This stripping can either be caused by mass transfer in a binary system or result from mass loss through strong stellar winds. As such, Type IIb SNe are sensitive probes of mass-loss processes, particularly of binary interactions (e.g Maund et al. 2004, Fox et al. 2014).

A number of progenitors of CCSNe have been imaged (see Smartt 2009 for a review) and explosion models are extensively discussed in the literature (e.g see the reviews of Janka 2012; Burrows 2013). SNe in other galaxies are unresolved at early times, but spectropolarimetry is a unique tool that can probe the 3D shape of young SN ejecta and thus provide constraints on the explosion models.

The opacity of the photosphere at early days is dominated by electron scattering (Shapiro & Sutherland 1982). As a result, the outgoing radiation has a polarization vector perpendicular to the

★ E-mail: fstevance1@sheffield.ac.uk
† Royal Society Research Fellow

plane of last scattering (i.e. containing the incident and scattered ray). Additionally, the amplitude of the polarization quasi-vector increases with distance to the centre from the ejecta projected on to the plane of the sky (Chandrasekhar 1946). In a spatially unresolved envelope with central symmetry (e.g spherical), the polarization components will cancel fully, resulting in null integrated polarization. Departure from spherical symmetry, however, will result in incomplete cancellation and a polarization excess (Shapiro & Sutherland 1982; McCall 1984), which can be measured to probe the shape of the SN ejecta. Deviations from central symmetry can be the result of a photospheric geometry (Höflich 1991), off-centre energy sources (Chugai 1992; Höflich 1995), or partial occultation of the underlying photosphere by a non-isotropic distribution of the line-forming regions (e.g. Kasen et al. 2003). Additionally, non-zero polarization can be the result of scattering by circumstellar dust (Wang & Wheeler 1996).

Practically all CCSNe show net intrinsic polarization (Wang & Wheeler 2008). Despite their relatively low rates (∼12 per cent of CCSNe, Eldridge et al. 2013), Type IIb SNe are surprisingly well represented in the spectropolarimetry literature and have shown a range of behaviours. Most Type IIb SNe – such as SN 1993J, SN 1996cb, SN 2008ax, SN 2008aq, or SN 2011dh – have continuum polarization around $p \sim 0.5$ per cent to ~ 1 per cent (Trammell, Hines & Wheeler 1993; Wang et al. 2001; Chornock et al. 2011; Silverman et al. 2009; Stevance et al. 2016; Mauerhan et al. 2015). Some Type IIb SNe (e.g. SN 2001ig or SN 2008aq) exhibited a spectropolarimetric evolution similar to that of Type II-P SNe, where a lower continuum polarization was seen at early times and increased to $p > 1$ per cent by the time helium started dominating the spectrum (Leonard et al. 2006; Maund et al. 2007b; Stevance et al. 2016). SN 2011dh, on the other hand, exhibited a decrease in polarization from ∼0.75 per cent around maximum light to ∼0.2 per cent by 8 d after maximum. Additionally, strong line polarization of hydrogen, helium and calcium features is often detected in Type IIb SNe. The amplitude of the peaks can range from ∼0.5 per cent (e.g. SN 2001ig or SN 2011dh at early times) to above 3 per cent in SN 2008ax (Maund et al. 2007b; Mauerhan et al. 2015; Chornock et al. 2011).

Although Type IIb SNe are better represented than other types in the spectropolarimetric literature, the number of high-quality multi-epoch data sets remains limited. Increasing our sample is ultimately necessary to compare the statistical distribution of the observed polarization to available models (e.g. Höflich 1991; Kasen et al. 2003; Dessart et al. 2011; Tanaka et al. 2017).

In this work, we present seven epochs of spectropolarimetric and spectroscopic data for SN 2011hs observed with the Very Large Telescope (VLT) from −3 to +40 d with respect to *V*-band maximum (2011 November 22 – see Bufano et al. 2014). The observations are described in Section 2. A study of the interstellar polarization (ISP) in the line of sight of SN 2011hs is given in Section 3; we identify unusual levels of ISP and discuss potential implications for the dust in the host galaxy or in the vicinity of the SN. In Section 4, we analyse the intrinsic polarization of SN 2011hs. In Section 5, we compare the intrinsic polarization of SN 2011hs to that of previously studied Type IIb SNe and discuss potential interpretations. Finally, a summary is given in Section 6.

2 OBSERVATIONS AND DATA REDUCTION

SN 2011hs was discovered by Stuart Parker on 2011 November 12.476 and classified by Milisavljevic et al. (2011). It is located at RA = $22^{h}57^{m}11^{s}$ and δ = -43°23'04' in the galaxy IC 5267 (face-on sA0) with redshift $z = 0.005711$, corresponding to a recessional velocity of 1714 km s^{-1} (Koribalski et al. 2004). A series of spectropolarimetric observations of SN 2011hs were taken with the VLT of the European Southern Observatory (ESO) using the Focal Reducer and low-dispersion Spectrograph in the dual-beam spectropolarimeter mode (PMOS – Appenzeller et al. 1998). Linear spectropolarimetry was obtained for four half-wave retarder angles (0°, 22.5°, 45°, and 67.5°) at seven epochs between 2011 November 19 and 2012 January 01. A summary of observations is given in Table 1. All observations were performed with the 300V grism, providing a spectral resolution of 12 Å (as measured from arc-lamp calibration images). The GG435 order sorting filter was used to avoid contamination of our data by higher dispersion orders. Our data are thus limited to the wavelength range 4450–9330 Å. The spectropolarimetric data were reduced in the standard manner using IRAF[1] following the prescription of Maund et al. (2007a) and the Stokes parameters were calculated using FUSS (Stevance et al. 2017). The data acquired on 2011 November 19, November 24, and December 02 were binned to 15 Å, the data obtained on 2011 December 10 were binned to 30 Å and the data obtained at subsequent epochs were binned to 45 Å to increase the signal-to-noise ratio (S/N). The spectra were flux calibrated using the standard stars reported in Table 1 with the polarimetric optics in place in order to remove the instrumental response. It should be noted, however, that due to unknown slit losses, absolute flux calibration was not possible.

Table 1. VLT Observations of SN 2011hs. The epochs are given relative to the estimated *V*-band maximum.

Object	Date (UT)	Exp. time (s)	Epoch (d)	Airmass
SN 2011hs	2011 Nov. 19	8 × 850	−3	1.05–1.23
EGGR 141[a]	2011 Nov. 19	2 × 60	–	1.26
SN 2011hs	2011 Nov. 24	8 × 900	+2	1.1–1.36
EGGR 150[a]	2011 Nov. 24	2 × 191	–	1.31
SN 2011hs	2011 Dec. 02	8 × 900	+10	1.16–1.56
LTT1788[a]	2011 Dec. 02	2 × 60	–	1.04
SN 2011hs	2011 Dec. 10	8 × 900	+18	1.3–2.0
LTT1788[a]	2011 Dec. 10	2 × 60	–	1.8
SN 2011hs	2011 Dec. 16	4 × 855	+24	1.4–2.3
LTT1788[a]	2011 Dec. 16	2 × 120	–	1.14
SN 2011hs	2011 Dec. 23	4 × 1100	+31	1.4–1.77
LTT1788[a]	2011 Dec. 23	2 × 60	–	1.034
SN 2011hs	2012 Jan. 01	4 × 1100	+40	1.6–2.1
LTT1788[a]	2011 Dec. 16	2 × 120	–	1.14

Note. [a]Flux standard.

2.1 Observed flux and spectropolarimetry

2.1.1 Flux spectrum and photospheric velocity

In Fig. 1, we present the observed spectropolarimetry and flux spectrum at seven new epochs for SN 2011hs.

[1]IRAF is distributed by the National Optical Astronomy Observatory, which is operated by the Association of Universities for Research in Astronomy (AURA) under a cooperative agreement with the National Science Foundation.

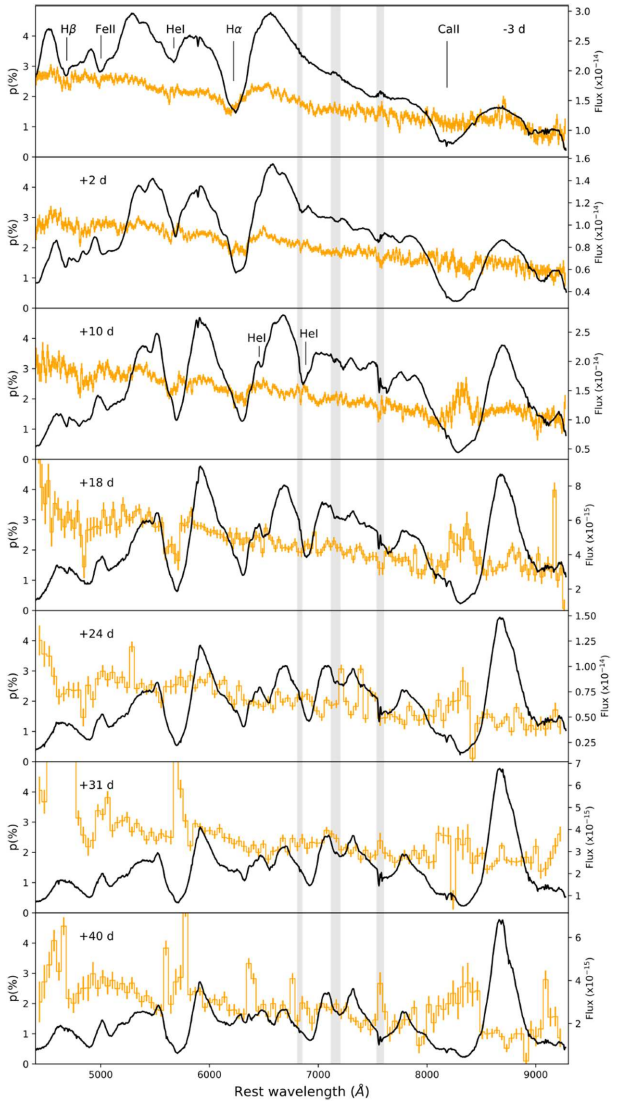

Figure 1. Flux spectrum (black) and degree of polarization (not corrected for ISP – orange) of SN 2011hs ranging from −3 to +40 d. The grey shaded areas represent the regions affected by telluric lines. The data at −3, +2, and +10 d were binned to 15 Å, the data at +18 d were binned to 30 Å, and the following epochs were binned to 45 Å. Note that the strong peaks of polarization near 4600 and 5700 Å at +31 and +40 d are not considered to be real (see Section 2.1.2).

As noted by Bufano et al. (2014), early epochs of spectroscopy are dominated by Hα (−3 d), but as the SN evolves through maximum light the feature decreases in strength and a blue shoulder appears (+2 d). We also see that from a week after maximum, the spectrum is dominated by He I features. An exhaustive spectroscopic analysis is beyond the scope of this paper, and more details on the spectroscopy of SN 2011hs and comparison to other SNe can be found in Bufano et al. (2014). Nonetheless, for the needs of this work we estimate the photospheric velocities at the time of observations (see Section 4). The velocities of the Fe II lines in the blue part of the spectrum can be used as a proxy to probe photospheric velocity (e.g Bufano et al. 2014), so we perform fits of Fe II λ5169 at all epochs in order to find the absorption minima. The resulting velocities are given in Table 2, and are consistent with the estimates of Bufano et al. (2014) from fits of the same line, see their fig. 9.

Table 2. Line velocities at the absorption minimum for Fe II λ5169 at all epochs, which is used as a proxy for photospheric velocity.

Epoch (d)	Fe II (km s^{-1})
−3	−9860
+2	−8760
+10	−6320
+18	−5570
+24	−5390
+31	−4810
+40	−4470

2.1.2 *Observed polarization*

As seen in Fig. 1, we detect significant polarization in the direction of SN 2011hs, showing an underlying slope with a higher degree of polarization at the blue end of the spectrum (∼3 per cent) than at the red end (∼1 per cent). This behaviour is not expected for the continuum polarization of SNe since Thomson scattering is wavelength independent. Additionally, some excess polarization is associated with the absorption component of Ca II from 10 d after *V*-band maximum, and polarization troughs are seen corresponding to Hα at the first three epochs, as well as with He λ5876 at +10 and +18 d. The presence of troughs is inconsistent with the expected correlation of polarization peaks with absorption components (e.g Wang & Wheeler 2008). These discrepancies seem to indicate that ISP contributes very significantly to the continuum polarization observed (see Section 3 for a more complete discussion).

Lastly, it should be noted that the strong peaks near 4600 and 5700 Å at +31 and +40 d are coincident with significant variations from zero in our instrumental signature correction $\Delta\varepsilon$ (see Maund 2008), reducing our confidence in our data at these wavelengths. Spectral extraction using the non-optimal method was attempted to test whether a failure of the optimal extraction algorithm could be responsible for such wide anomalies. This method, however, showed the same peaks. A similar spurious feature over a wide wavelength range has also been encountered in the spectropolarimetric data of WR102 (Stevance et al. 2018), but its origin could not be identified. We do not consider these peaks to be intrinsic to the SN or to the ISP, and they will therefore not be considered in our analysis.

3 INTERSTELLAR POLARIZATION

3.1 Galactic ISP

In order to estimate the contribution of the Galactic ISP we searched for Milky Way field stars in the vicinity of SN 2011hs. If we assume that they are intrinsically unpolarized, any polarization measured for these stars is due to Galactic ISP. In the Heiles (2000) catalogue, we found two stars within 2 deg of SN 2011hs: HD218227 and HD215544 with polarization $p = 0.012$ and 0.116 per cent, respectively. Using the parallaxes found in the *Gaia* data release DR2 (Luri et al. 2018), we calculate distances of 36.1 ± 0.7 and 501 ± 10 pc for HD218227 and HD215544, respectively. HD218227 being such a nearby object explains its low polarization degree compared to HD215544, and the latter better samples the Galactic dust column and the ISP in the direction of SN 2011hs.

It is possible to put an upper limit on the Galactic ISP following $p_{\max} < 9 \times E(B-V)$ (Serkowski 1973). The Galactic reddening in the direction of SN 2011hs is $E(B-V) = 0.011 \pm 0.002$ (Schlafly & Finkbeiner 2011), yielding $p_{\rm ISP} < 0.099 \pm 0.018$ per cent. The polarization of HD215544 is at the upper end of this limit (within

uncertainties). This is much lower than the observed polarization and the Galactic ISP is therefore a small contribution to the total observed ISP.

3.2 Estimating the ISP

In order to estimate the ISP from our observations, some assumptions must be made. Any such estimate is inevitably model dependent. In the following section, we present three different methods we employed to determine the ISP.

3.2.1 ISP determined from the polarization associated with emission lines

(i) Assuming that the SN polarization is null in the wavelength ranges corresponding to strong emission lines (e.g Stevance et al. 2016) can help us quantify the ISP. If we consider the Stokes parameter q (similar equations are used for u), the total polarization $q_{\rm tot}$ across a line will follow:

$$q_{\rm tot}F_{\rm tot} = q_{\rm line}F_{\rm line} + q_{\rm cont}F_{\rm cont} \quad (1)$$

Here $q_{\rm line}$ is the polarization associated with the emission component, $q_{\rm cont}$ is the continuum polarization, and the total flux across the line is the sum of the line flux and continuum flux: $F_{\rm tot} = F_{\rm line} + F_{\rm cont}$. Since we assume no intrinsic polarization from the SN in the wavelength ranges corresponding to strong emission line, $q_{\rm line}$ is effectively $q_{\rm ISP}$.

We first attempted to extract the ISP from our earliest epochs (−3, +2, and +10 d) of spectropolarimetry since they have better S/N. Additionally, we expect our ISP estimates from the Hα line to be more robust at early dates when He I is still weak. In order to retrieve $q_{\rm line}$ (i.e. $q_{\rm ISP}$) from equation (1), we re-arranged to obtain

$$\frac{q_{\rm tot}F_{\rm tot}}{F_{\rm cont}} = q_{\rm line} \times \frac{F_{\rm line}}{F_{\rm cont}} + q_{\rm cont}, \quad (2)$$

which is the expression of a straight line whose gradient is $q_{\rm line}$ and intercept is $q_{\rm cont}$. We then extracted the values of $q_{\rm tot}$ and $F_{\rm tot}$ at each wavelength bin in the range associated with the strong emission component. In order to find $F_{\rm cont}$, we visually selected spectral regions of continuum on either side of the emission line and traced a straight line across the spectral feature, giving us $F_{\rm cont}$ at each wavelength bin. By far, this process was the most difficult and the greatest source of inaccuracy. We plotted $\frac{q_{\rm tot}F_{\rm tot}}{F_{\rm cont}}$ against $\frac{F_{\rm line}}{F_{\rm cont}}$ for each wavelength bin in the emission line range, and fitted the points using Orthogonal Distance Regression (ODR).

We used this technique with the blue iron complex, Hα, and Ca II. In the case of SN 2011hs, the ISP is not constant but a function of wavelength, which in the range of interest (4500–9300 Å) is assumed to be linear. Hence, fitting the values of $q_{\rm isp}$ against wavelength with a straight line would in principle allow us to retrieve the ISP–wavelength relationship. When applying this method to epochs 1–3, however, the fits were found to be poor and inconsistent with each other. This could indicate that our assumptions were inadequate, or it could be the result of the great uncertainties associated with the approximation of the continuum flux.

(ii) Another approach is to consider the polarization in the spectral regions corresponding to strong emission lines at a later time, here epoch 7 (+40 d). By then intrinsic polarization and continuum flux had significantly decreased, therefore for strong emission lines $F_{\rm line} \gg F_{\rm cont}$. In this limit, $F_{\rm tot}/F_{\rm line} \rightarrow 1$ and $q_{\rm line}F_{\rm line}$

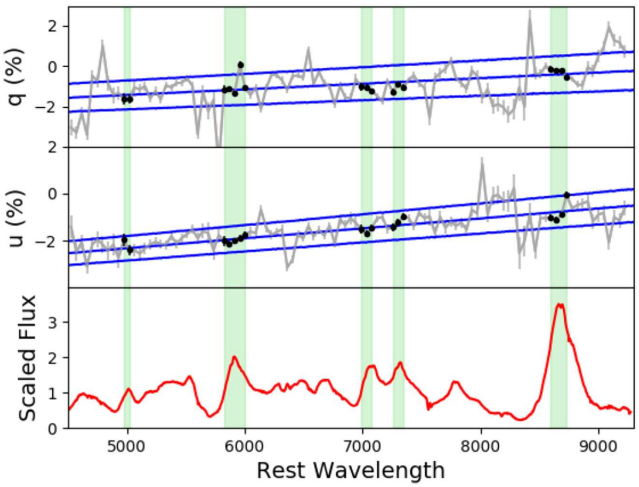

Figure 2. Linear regression (blue) of the Stokes parameters q and u at +40 d in the wavelength range corresponding to emission lines (green highlight). The fitted points are shown in black. The 1σ lines above and below the fits were determined using Monte Carlo sampling of the gradient and intercept of $q_{\rm ISP}$ and $u_{\rm ISP}$ within their errors. The flux spectrum at +40 d is shown in red.

$\gg q_{\rm cont}F_{\rm cont}$. Consequently, equation (2) simplifies to $q_{\rm line} = q_{\rm tot}$. Once again $q_{\rm line}$ is equivalent to $q_{\rm ISP}$.

In order to derive the ISP–wavelength relationship, we isolated the Stokes parameter values in the following wavelength ranges: 4970–5020, 5825–6000, 6985–7075, 7255–7345, and 8600–8730 Å, see Fig. 2. We performed an ODR fit, yielding:

$$q_{\rm ISP}\,(\text{per cent}) = 2.76(\pm0.80) \times 10^{-4} \times \lambda - 2.80(\pm0.59), \quad (3)$$

$$u_{\rm ISP}\,(\text{per cent}) = 4.21(\pm0.59) \times 10^{-4} \times \lambda - 4.42(\pm0.43), \quad (4)$$

where λ is in Å, the gradients have units of Å^{-1} and the intercepts are unitless.

When estimating the ratio of line to continuum flux in the spectral region of the calcium infrared (IR) triplet (our strongest line), however, we find that $F_{\rm line} \sim 3 \times F_{\rm cont}$. Consequently, assuming that the potentially polarized continuum flux is negligible in the region of the emission lines is debatable. We therefore employ another, independent, method to estimate the ISP.

3.2.2 ISP determination from late time data

In the context of electron scattering by the SN ejecta, at late times, the polarization intrinsic to the SN will tend towards zero, since the electron density decreases as the ejecta expand, and the observed polarization therefore tends toward that of the ISP. By assuming complete depolarization at our last epoch (+40 d) and fitting a straight line to the normalized Stokes parameters q and u, the wavelength dependent $q_{\rm ISP}$ and $u_{\rm ISP}$ can then be found (see Fig. 3). The best results were obtained when using the original data at +40 d (not rebinned to 45Å), where spurious points were removed according to their corresponding $\Delta\varepsilon$. Data points whose $\Delta\varepsilon$ showed a 3σ or greater deviation from zero were not included in our fits.

The resulting ISP–wavelength relationships are:

$$q_{\rm ISP}\,(\text{per cent}) = 2.63(\pm0.19) \times 10^{-4} \times \lambda - 2.68(\pm0.14), \quad (5)$$

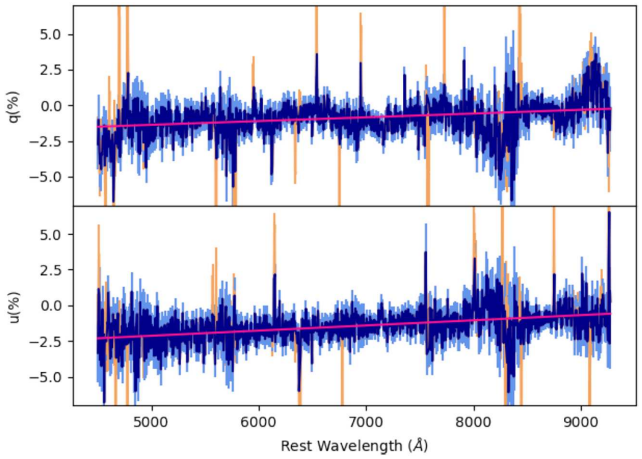

Figure 3. Stokes parameters q and u at +40 d (dark blue; errors in light blue) 3σ-clipped according to $\Delta\varepsilon$; the discarded points are shown in orange. The bin size for the data is 3.3 Å. The fits to the σ-clipped data are shown in magenta.

$$u_{\rm ISP}\,(\text{per cent}) = 3.61(\pm0.17) \times 10^{-4} \times \lambda - 3.94(\pm0.12), \qquad (6)$$

where λ is in Å, the gradients have units of Å^{-1}, and the intercepts are unitless. The reduced chi-squared (χ^2_ν) values on the q and u fits were 1.39 and 0.93, respectively. The fits are therefore satisfactory. Additionally, the parameters derived here are consistent with equations (3) and (4). Consequently, we are confident in our ISP estimate. We chose to use equations (5) and (6) for ISP removal to avoid the propagation of the large uncertainties associated with equations (3) and (4) on to our ISP removed data. The intrinsic polarization of SN 2011hs is presented and analysed in Section 4.

3.3 Host galaxy of SN 2011hs and Serkowski law

From the upper limits on the Galactic ISP derived in Section 3.1, we can conclude that most of the ISP in the data of SN 2011hs originated from IC 5267. Under the assumption that the size and composition of interstellar dust grains are similar in the host galaxy of SN 2011hs as they are in the Milky Way, the Serkowski limit $p_{\rm ISP} < 9 \times E(B-V)$ can be applied to derive a value for the maximum $p_{\rm ISP}$. In order to do so, a value for the reddening of IC 5267 must be calculated. To this end, we measured and averaged the equivalent widths of the Na I D line in the data of epochs 1–3 (at later epochs, the blend of sodium with He I made our equivalent width measurements unreliable). We then used the relationship between equivalent width and reddening described by Poznanski, Prochaska & Bloom (2012), and calculated $E(B-V)_{\rm host} = 0.11\,(\pm0.02)$. According to Serkowski (1973), this yields $p_{\rm ISP} < 1.09\,(\pm0.18)$. At 5000 Å, however, we find $p_{\rm ISP} = 2.50(\pm\ 0.15)$ per cent, as calculated from $q_{\rm ISP}$ and $u_{\rm ISP}$ derived in Section 3.2.2. Therefore, the assumption that the dust of IC 5267 or in the vicinity of SN 2011hs is similar to that of the Milky Way may not be correct. It is however worth noting that the Na ID lines are caused by discrete gas clouds and do not probe the more diffuse interstellar medium (ISM), therefore only providing a lower limit on the dust extinction. Consequently, the Poznanski et al. (2012) estimate may not be completely adequate.

Another approach is to fit our data at +40 d with the Serkowski law (Serkowski, Mathewson & Ford 1975):

$$p(\lambda) = p_{\rm max} \exp\left[-K \ln^2\left(\frac{\lambda_{\rm max}}{\lambda}\right)\right], \qquad (7)$$

where K is a constant, $p_{\rm max}$ is the maximum polarization, and $\lambda_{\rm max}$ is the wavelength at polarization maximum. We attempted to find new values of the parameters $p_{\rm max}$ and $\lambda_{\rm max}$ by minimizing the χ^2 to better fit our data. Two forms of the constant K were considered: the original value derived by Serkowski et al. (1975) $K_{\rm S} = 1.15$, and the $\lambda_{\rm max}$ dependent form of Whittet et al. (1992) $K_{\rm W} = 0.01 + 1.66\lambda_{\rm max}$.

The normalized Stokes parameters q and u can be expressed as functions of the wavelength dependent degree of polarization $p(\lambda)$ and the polarization angle (P.A.) θ as

$$q(\lambda) = p(\lambda)\cos(2\theta) \text{ and } u(\lambda) = p(\lambda)\sin(2\theta), \qquad (8)$$

where $p(\lambda)$ is defined by equation (7) and here $\theta = 120^\circ$ (as from equations 5 and 6, the P.A. θ is found to be $120^\circ \pm 2^\circ$ across our wavelength range). Note that we did not attempt to remove the Galactic component, since it is <0.1 per cent and therefore contributes very little to the total ISP.

The fits to q, u, and p performed using $K_{\rm S}$, as well as values of χ^2_ν in parameter space are shown in Fig. 4. The values of the reduced chi-squared (16.4 at best) indicate a relatively poor fit, and the size of the 1σ and 3σ contours in Fig. 4 reflect the uncertainty on the best parameter values. Nevertheless, it is possible using the 3σ contours to put limits on $p_{\rm max}$ and $\lambda_{\rm max}$. We find that 2090 Å < $\lambda_{\rm max}$ < 4245 Å and 2.24 per cent < $p_{\rm max}$ < 7.55 per cent, with 99.7 per cent confidence.

We also fitted a Serkowski law with $K_{\rm W}$ (Whittet et al. 1992), as shown in Fig. 5, along with the plot of χ^2_ν in parameter space. Once again, the reduced chi-squared shows that the fit is relatively poor and the 1σ contour covers a large portion of parameter space. We can however put limits on the values of $p_{\rm max}$ and $\lambda_{\rm max}$ from the 3σ contour: 690 Å < $\lambda_{\rm max}$ < 4700 Å and 1.88 per cent < $p_{\rm max}$ < 3.66 per cent with 99.7 per cent confidence.

3.4 Applicability of Serkowski's law

The χ^2_ν values across parameter space showed very large 1σ contours, encompassing many $p_{\rm max}$–$\lambda_{\rm max}$ pairs. This is mostly due to the fact that the $\lambda_{\rm max}$ peak is not in the wavelength range covered by our observations, hence making it difficult to better constrain the fit. The limits placed on the values of $\lambda_{\rm max}$ extended well beyond the optical range into the far-ultraviolet (far-UV). This is a concern as Serkowski's law was empirically defined from optical data (Serkowski et al. 1975), and it has been found that the law is not necessarily applicable in the UV (e.g. Anderson et al. 1996; Martin, Clayton & Wolff 1999; Patat et al. 2015). Furthermore Martin et al. (1999) explain that the Serkowski equation (see equation 7) is not flexible enough to provide adequate fits all the way from UV to IR for a given K, and that often performing a three parameters fit to find $p_{\rm max}$, $\lambda_{\rm max}$, and K gives better results. Patat et al. (2015) applied this method, and for the case of SN 2006X found $K = 1.47 \pm 0.05$, which is very different from $K_{\rm W}$ and $K_{\rm S}$ which we used for our fits. Therefore, fitting data which peak in the UV with optical Serkowski laws, as is done here, may not be adequate.

The very different shapes of the χ^2_ν contours in parameter space for the two values of K used in this work (see Figs 4 and 5) shows the importance of the choice of K. Given the nature of our data, in particular the fact that $\lambda_{\rm max}$ is visibly outside of the range we

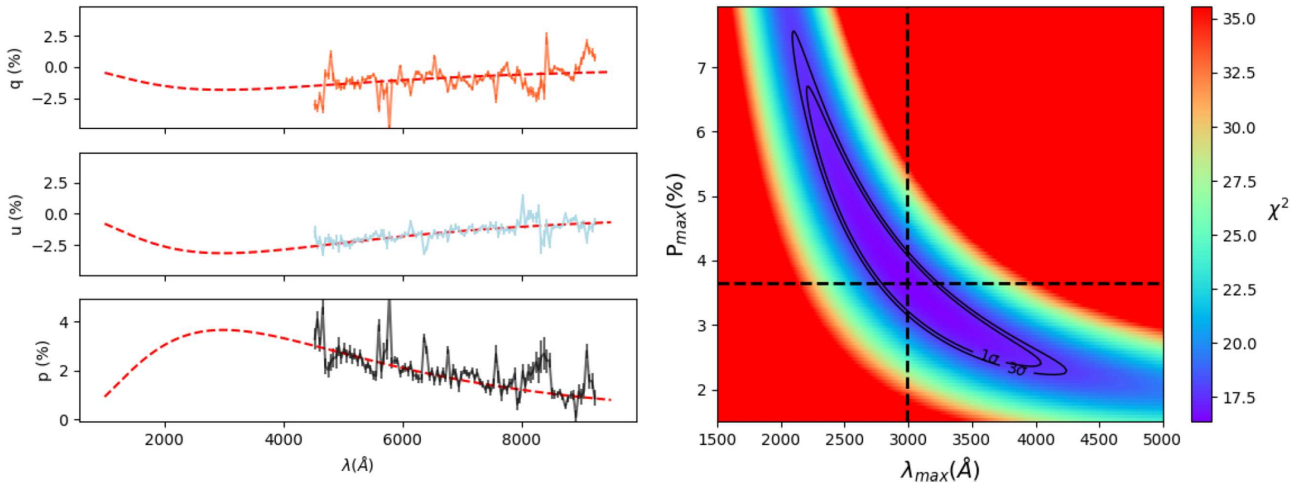

Figure 4. Left-hand panel: the red dashed lines represent the Serkowski law fits ($K = 1.15$) to the normalized Stokes parameters q and u at +40 d, and the corresponding fit to p. Right-hand panel: Reduced χ^2 in parameter space. The 1σ and 3σ contours are plotted as thick black lines, the dashed lines indicate the values of $p_{\max}$ and $\lambda_{\max}$ for which χ^2_ν is minimized. The colour scale shows the evolution of χ^2_ν in parameter space.

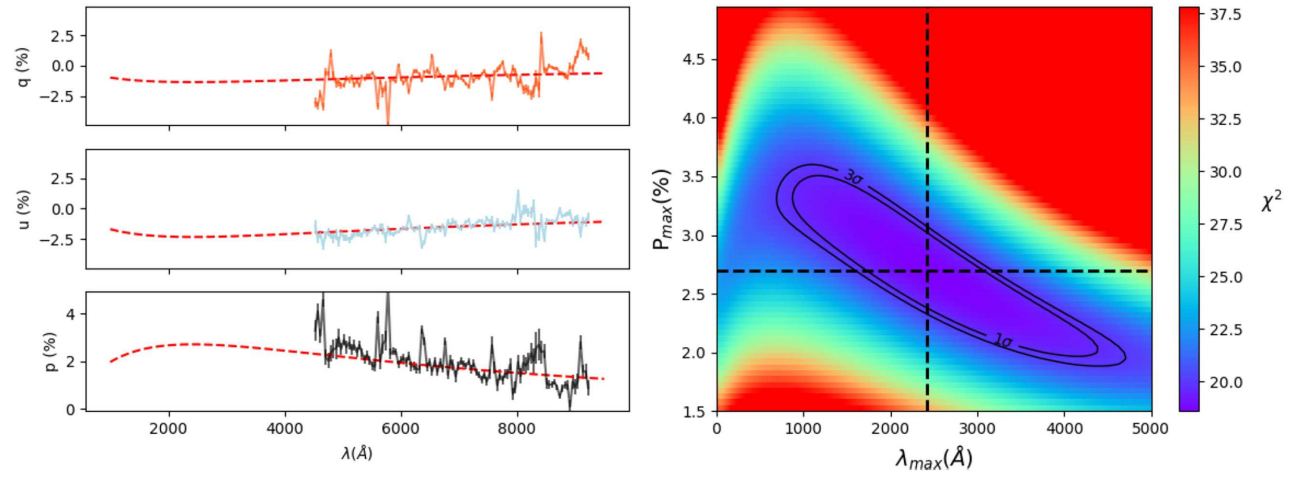

Figure 5. Left-hand panel: the red dashed lines represent Serkowski law fits ($K = 0.01 + 1.66\lambda_{\max}$) to the normalized Stokes parameters q and u at +40 d, and the corresponding fit to p. Right-hand panel: reduced χ^2 in parameter space. The 1σ and 3σ contours are plotted as thick black lines, and the dashed lines indicate the values of $p_{\max}$ and $\lambda_{\max}$ for which χ^2_ν is minimized. The colour scale shows the evolution of χ^2_ν in parameter space.

cover, a three parameter fit cannot help constrain our estimate of the parameters.

On the whole, the observed polarization curves are very different from what is expected from Galactic-type ISP. Furthermore, it is anticipated that the ISP P.A. should be parallel to the local spiral arm of the host galaxy at the location of the SN, due to the alignment of the dust with the magnetic field of the host. However, the ISP angle of $\sim 120^\circ$ is found not to be parallel to the local spiral arm (see Fig. 6). This could suggest that the dust in IC 5267 or in the local neighbourhood of SN 2011hs maybe different from that in the Milky Way.

An alternative explanation to the observed ISP profile and P.A. is the presence of circumstellar dust. Polarization curves increasing at blue wavelengths and with $\lambda_{\max} < 4000$ Å have been see in Type Ia SNe (e.g 1986G, SN 2006X, and SN 2014J – Patat et al. 2015). Hoang (2017) modelled the observed polarization curves and extinction and found this behaviour to be the result of an enhancement in small silicate grains in the dust. They suggest this could be due to cloud–cloud collisions resulting from SN radiation pressure. Alternatively Hoang et al. (2018) show that large silicate grains can be destroyed by strong radiation fields such as those around massive stars and SNe. Additionally, Cikota et al. (2017), remarked that the polarization curves of Type Ia SNe are similar to those of protoplanetary nebulae, that are produced by scattering in the circumstellar medium. Consequently, the peculiar ISP found in the observations of SN 2011hs may hint at the presence of circumstellar dust around the SN.

4 INTRINSIC POLARIZATION

The degree of polarization of SN 2011hs after ISP correction (see Section 3) is shown alongside the flux spectrum in Fig. 7.

We derived the degree of polarization and P.A. for the prominent polarization features and the continuum where possible. Each value in this table is associated with a particular wavelength or wavelength range. In the former case, we simply recorded the polarization at the corresponding wavelength bin, whereas when a range is provided we averaged the values within that range and used the

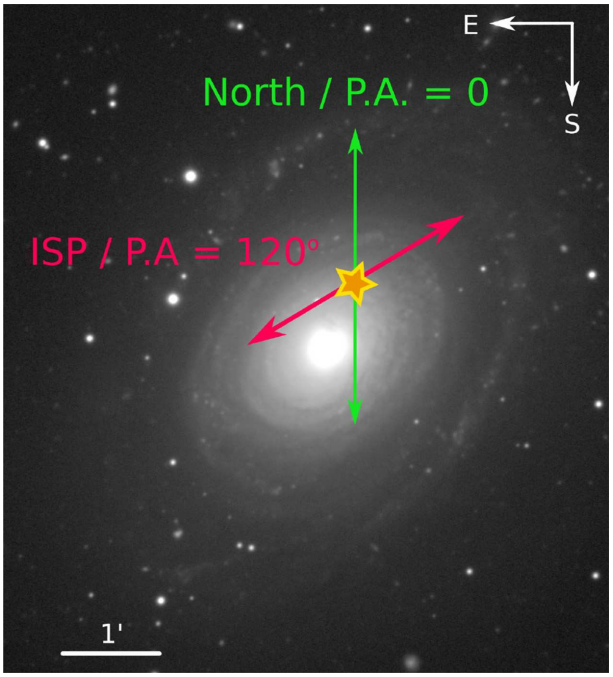

Figure 6. Orientation of the ISP P.A. at the location of SN 2011hs (marked by the star) in IC 5267. The image of the host galaxy is a *B*, *V*, *R*, and *I* composite from the Carnegie-Irvine Galaxy Survey (Ho et al. 2011).

standard deviation as the error. In order to estimate the continuum polarization, we average the polarization values in spectral regions devoid of strong lines and telluric lines. We could only find suitable regions of the spectra in epochs 1–4, and the wavelength ranges considered are indicated by the green lines in Fig. 7. The precise ranges used, and the continuum polarization and P.A. derived can be found in Table 3.

The continuum polarization is found to be constant within errors at epochs 1 and 2, with $p = 0.55 \pm 0.12$ per cent and 0.75 ± 0.11 per cent, respectively. At those dates the P.A. of the continuum is also constant within the error ($170° \pm 7°$ and $158° \pm 4°$ at -2 and $+3$ d, respectively). The degree of polarization then decreases to $p = 0.48 \pm 0.09$ per cent by $+10$ d and $p = 0.29 \pm 0.18$ per cent by $+18$ d, and a significant rotation of the P.A. is also observed ($141° \pm 7°$ and $120° \pm 9°$ at $+10$ and $+18$ d, respectively).

Prominent polarization features of He λ5876 are seen in Fig. 7 from -3 to $+18$ d with degree of polarization as high as $p = 1.08 \pm 0.36$ per cent at the latter epoch. The P.A. of helium follows that of the continuum at the first three epochs (see Table 3), but a sudden ∼90° rotation is seen from $+10$ to $+18$ d (from 141° to 54°, respectively).

The Hα polarization at -3 and $+2$ d exhibits a very broad feature extending from ∼5700 to ∼6300 Å. The broad hydrogen profile rises to $p = 0.75 \pm 0.08$ per cent in the first epoch (see Fig. 7 and Table 3). By $+2$ d, two distinct peaks can be seen centred around 6125 and 6260 Å, which share the same degree of polarization within errors ($p = 0.89 \pm 0.10$ per cent and 0.87 ± 0.08 per cent, respectively). These two peaks become better defined at $+10$ d, as the underlying broad profile fades, although their amplitude is seen to decrease by ∼0.3 per cent with respect to epoch 2. In subsequent epochs, no significant hydrogen feature is detected above the noise. Over time Hα exhibits a decrease in P.A., as seen with helium and the continuum.

Calcium shows by far the most prominent polarization features at all epochs, and is the only element to continue exhibiting polarization above noise levels up to our last epoch at $+40$ d (see Fig. 7 and Table 3). The amplitude of the feature remains roughly constant from -3 to $+24$ d, between 1 and 1.5 per cent, although the P.A. is seen to slowly decrease overtime. In the last two epochs, however, the polarization degree is well above the 1.5 per cent level, and a change in the evolution of the P.A. is also seen, as between $+31$ and $+40$ d it increases by 60°.

4.1 Polar plots

To help visualize the behaviour of the P.A. in velocity space, we create polar plots, which are diagrams showing the relative positions of the P.A. associated with strong polarization features. They were first proposed by Maund et al. (2009), and use the radial velocity position and the angle on the plane of the sky as coordinates. In Fig. 8, we show the polar plots at all epochs for helium, hydrogen, and calcium. Note that the data were binned for better visualization; the centres of the bins are the average P.A. calculated within the range. The angular extent of the bin on the polar plot represents the error, so that a larger angular extent shows greater uncertainty on the P.A. for a particular line, not a greater physical extent.

The locations of the continuum shown on Fig. 8 for epochs 1–4 correspond to the P.A. calculated for the continuum values given in Table 3. Unfortunately, the continuum polarization could not be formally calculated at the last three epochs, since we could not isolate spectral regions devoid of strong lines. We attempted to estimate the P.A. of the continuum by identifying its possible locus in $q - u$ space (see Section 4.2 and Fig. 9) by using a 2σ clipping method to eliminate outliers and the contribution of strong lines. This method was successfully used for the data at $+24$ and $+31$ d, yielding angles of $99° \pm 39°$ and $98° \pm 25°$, respectively. This is consistent with an absence of rotation from $+18$ to $+24$ and $+31$ d. At the last epoch, the average values of q and u and their standard deviations are consistent with null continuum polarization.

The change in P.A. of the continuum described in the previous section is visualized as a progressive clockwise rotation that takes place at epochs 2–4. Additionally, the P.A. of helium, hydrogen, and calcium clearly follow the clockwise rotation of the continuum over time, apart from He λ5876 at $+18$ d. In Section 4, we highlighted the 90° rotation of this feature from $+10$ to $+18$ d. This behaviour is clearly seen in Fig. 8, as at $+18$ d, the He λ5876 bins now fall into the upper quadrant, when the helium data were located in the bottom quadrant at $+2$ and $+10$ d. It is also very distinct from the behaviour of the other line features and the continuum.

4.2 $q - u$ plane

In Figs 9 and 10, we show the ISP corrected polarization data of SN 2011hs plotted on the Stokes $q - u$ plane. This is a very useful tool to try to understand the geometries of the ejecta (Wang et al. 2001). Bi-axial geometries will result in a linear structure of the polarization data on the $q - u$ plane. More complex geometries (such as the addition of a third axis of symmetry) will cause departures from such an alignment, sometimes in the form of a smooth rotation of the P.A. across the wavelength range of spectral lines, i.e. loops (Wang & Wheeler 2008). Potential physical causes for these geometries and interpretations of the $q - u$ plots will be discussed in Section 5.1.

The spectropolarimetric data of SN 2011hs at -3, $+2$, and $+10$ d show elongated ellipses on the $q - u$ plane, and the data were fitted with a dominant axis by performing ODR over the whole data

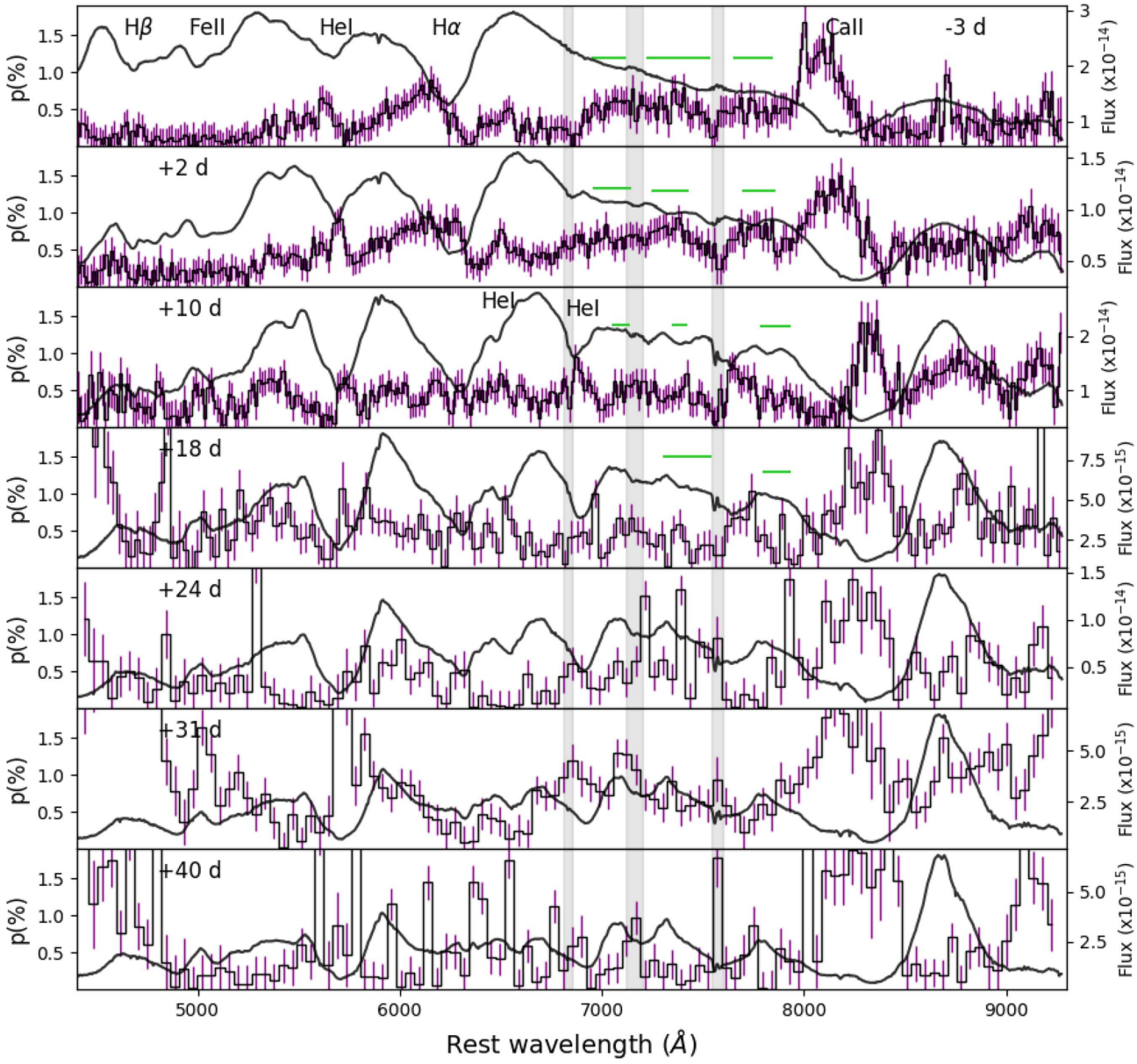

Figure 7. Degree of polarization (corrected for ISP) of SN 2011hs ranging from −3 to +40 d (purple). The flux spectrum is shown in black, the light grey shaded areas highlight the regions of telluric lines, and the green horizontal lines show the wavelength ranges used to calculate the continuum polarization. The data at −3, +2, and +10 d were binned to 15 Å, the data at +18 d were binned to 30 Å, and the following epochs were binned to 45 Å. Note that the strong peaks of polarization near 4600 and 5700 Å at +31 and +40 d are not considered to be real (see Section 2.1.2).

range. The lines of best fit at −3, +2, and + 10 d were found to have inclinations on the $q - u$ plane of 8.3 ± 1.4°, 172.3 ± 1.4°, and 169.6 ± 2.2°, respectively. Therefore, a clockwise rotation is observed in the orientation of the dominant axis as well as in the continuum P.A. (see Fig. 8 and Table 3).

The data at epochs 4–7 (+18 to +40 d) have a lower S/N and show no significant alignment along a dominant axis. The data at +18, +24, and +31 d present no significant elongation, but their slight offset from the origin of the $q - u$ plane is due to a residual level of intrinsic polarization. At +40 d, no elongation is seen and the data are centred around the origin, which is expected since it was used to quantify the ISP.

In order to look for departures from bi-axial geometry it is worth isolating the spectral regions corresponding to strong lines and seek loops. In Fig. 10, we show the $q - u$ plots of Ca II, Hα, and He λ5876. The calcium data at the first two epochs follow a clear linear configuration. A striking evolution is then seen between +2 and +10 d, with the appearance of a loop; loops are seen at all subsequent epochs. This evolution indicates that at early days the calcium polarization probes a bi-axial geometry and a third axis comes into play at epoch 3, resulting in the loops seen at and after +10 d. Hydrogen, on the other hand, shows the clearest loop at −3 d, where the Hα line is strongest. This indicates a break of the bi-axial geometry by hydrogen that is not shared by the calcium.

Table 3. Summary of the polarization and P.A. of the continuum and strong lines of SN 2011hs by epoch.

Epoch (d)	p in per cent (wavelength range)	P.A.
	Continuum	
−3	0.55 ± 0.12 (6955-7115 / 7225-7530/7655–7840)	170° ± 7°
+2	0.75 ± 0.11 (6960-7140 / 7250-7425/7700–7850)	158° ± 4°
+10	0.48 ± 0.09 (7055-7130 / 7350-7415/7790–7930)	141° ± 7°
+18	0.29 ± 0.18 (7310-7535/7800–7925)	120° ± 9°
	He Iλ5876	
−3	0.59 ± 0.05 (5590–5670)	173° ± 8°
+2	0.89 ± 0.03 (5660–5715)	155° ± 4°
+10	0.57 ± 0.05 (5685–5771)	141° ± 10°
+18	1.08 ± 0.36 (5712)	54° ± 3°
	Hα	
−3	0.75 ± 0.08 (6070–6200)	5° ± 6°
+2	0.89 ± 0.10 (6085-6160) / 0.87 ± 0.08 (6225–6295)	167° ± 1° / 168° ± 3.4°
+10	0.62 ± 0.02 (6150-6200) / 0.59 ± 0.01 (6285–6305)	155° ± 3° / 163° ± 1°
	Ca II	
−3	1.17 ± 0.20 (8030–8180)	177° ± 4°
+2	1.25 ± 0.15 (8055–8250)	166° ± 4°
+10	1.20 ± 0.25 (8275–8375)	134° ± 7°
+18	1.35 ± 0.30 (8205–8415)	134° ± 13°
+24	1.30 ± 0.26 (8100–8400)	75° ± 23°
+31	1.79 ± 0.22 (8100–8300)	41° ± 18°
+40	1.64 ± 0.16 (8100–8300)	107° ± 19°

Lastly, as the helium lines suddenly strengthen in the flux spectrum by +2 d, a loop also becomes visible in the wavelengths associated with He λ5876. This loop becomes more prominent by +10 d.

The observables presented are discussed and compared to those of other IIb SNe in the following section.

5 DISCUSSION

5.1 Potential interpretations for the polarization

Before we offer potential interpretations for the polarization of SN 2011hs, we summarize how the polarization is understood to probe the ejecta geometry as well as some literature base cases. We will then place the observational properties described in Section 4 within this framework.

As mentioned in the Introduction, the opacity in SN ejecta is dominated by electron scattering, causing the light to be polarized with a vector tangential to the photosphere at the point of scattering. After a few hours to a few days with respect to the explosion, the ejecta can be assumed to be in homologous expansion ($r = v \times t$) in all directions. Consequently, the physical structure of the envelope does not change over time and variations in p, q, and u can be understood in terms of a receding photosphere in a hydrodynamically 'inactive' structure. Additionally, homologous expansion means that different wavelengths across a line feature will probe different 'velocity slices', which are flat projections on the sky. As a result of the flat projection of a 3D envelope, the outer regions of the projected structure will correspond to regions of the envelope with lower optical depth than the central regions. Furthermore, the degree of polarization is dependent on optical depth, as demonstrated by the Monte Carlo simulations of Höflich (1991).

In this picture, the integrated polarization of spherical unresolved ejecta is 0, whereas aspherical geometries result in incomplete cancellation of the Stokes parameters and a net polarization signal. The observed time-scales of variations in p and P.A., in combination with the Doppler shift of lines, provide a direct link between the observables and the structure of the envelope.

Polarization probes deviations from sphericity in both the structure of the photosphere and the direction of the radiation reaching the photosphere. This leads to three classical base cases:

(i) Aspherical electron distributions, such as an ellipsoidal photosphere, resulting in continuum polarization (van de Hulst 1957; Höflich 1991).

(ii) Partial obscuration of the underlying Thomson-scattering photosphere leading to line polarization (e.g Kasen et al. 2003).

(iii) Asymmetric energy input, e.g. heating by off-centre radioactive decay (Chugai 1992; Höflich 1995).

Naturally, several or all of these configurations can occur. These three base cases provide a framework within which to understand changes in the continuum P.A. over time, as well as loops on the q–u plane at specific epochs.

Changes in the continuum P.A. over time arise if the geometry of the ejecta is more complex than a simple bi-axial configuration. In the case of an ellipsoidal photosphere, for example, the overall evolution of the density gradient over time causes a change from a prolate to an oblate configuration, as the photosphere traverses layers with less steep density structures or a recombination front (Höflich, Wheeler & Wang 1999). This can be seen as a mixture of two case (i) scenarios (oblate + prolate), and this departure from the simple bi-axial geometry will result in a rotation in continuum P.A. across epochs. Another possible configuration causing such a rotation is a mixture of cases (i) and (iii), whereby the photosphere has a bi-axial geometry but an off-axis energy source also comes into play, resulting in a tri-axial geometry.

Rotation of the P.A. across spectral lines (loops) at a particular epoch can also be understood as being the result of a tri-axial component. In the mixture of cases (i) and (iii) described above (an off-axis energy source in a bi-axial photosphere), the change of P.A. with wavelength arises as a result of the frequency dependence of the

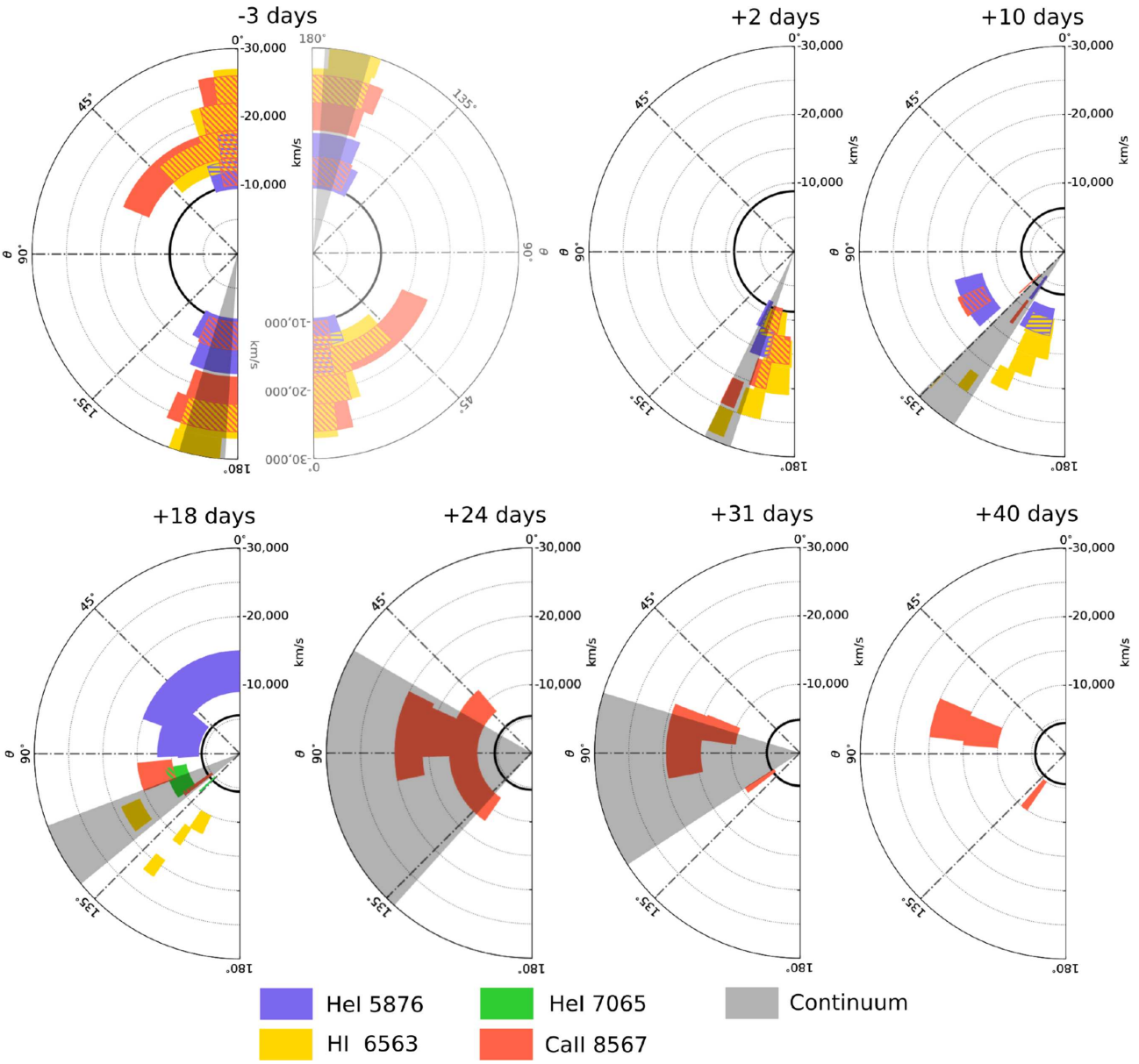

Figure 8. Polar plots of SN 2011hs from −3 to +40 d with respect to *V*-band maximum light. The P.A. of He I, Hα, and Ca II are shown as a function of radial velocity. The velocity of Fe IIλ5169 (proxy for photospheric velocity) is shown in black. The hatched areas represent the overlap between elements. The continuum P.A. is shown in grey. It should be noted that the apparent symmetry seen at −3 d is a consequence of the nature of the Stokes parameters being quasi-vectors. The upper and lower arcs are joined at the 0°–180° boundary, as shown by the faded addition of the rotated diagram of the −3 d plot.

thermalization depth (below which information about the geometry is lost due to multiple scattering – Höflich 1995). Alternatively, loops will also form if the distribution of the line forming region blocking the photosphere is not aligned with the symmetry axis created by an underlying bi-axial photosphere – case (i) + case (ii) – or by an off-centre energy source – case (ii) + case (iii).

In Section 4, the continuum polarization was seen to be significant and constant within errors at the first two epochs ($p = 0.55 \pm 0.12$ and $p = 0.75 \pm 0.11$ per cent at −3 and +2 d, respectively), but then decreases down to ∼0.3 per cent by +18 d (see Table 3). Simultaneously, the $q - u$ plots show significant elongation in the first two epochs, which then becomes less prominent by +10 d finally leading to an absence of a clear dominant axis by +18 d (see Fig. 9). This suggests that the ejecta initially show significant bi-axial geometry and overall appear more spherical at later dates. In the context of an oblate ellipsoid, the early time ejecta differs from sphericity by ∼10 per cent (Höflich 1991).

Now focusing on P.A., we saw in Table 3 and Fig. 8 that the continuum P.A. showed a gradual clockwise rotation (until +18 d, after which no precise estimate could be made). The average P.A. of the polarization features associated with helium, hydrogen, and calcium follow the behaviour of the continuum at the first four epochs (apart from He I λ5876 at +18 d, which we discuss below). Additionally, a clockwise rotation of the dominant axis is also seen in the $q - u$ planes between epochs 1 and 3. The homogeneous behaviour of the continuum and line polarization suggests that they are in some way coupled. In a scenario where line polarization

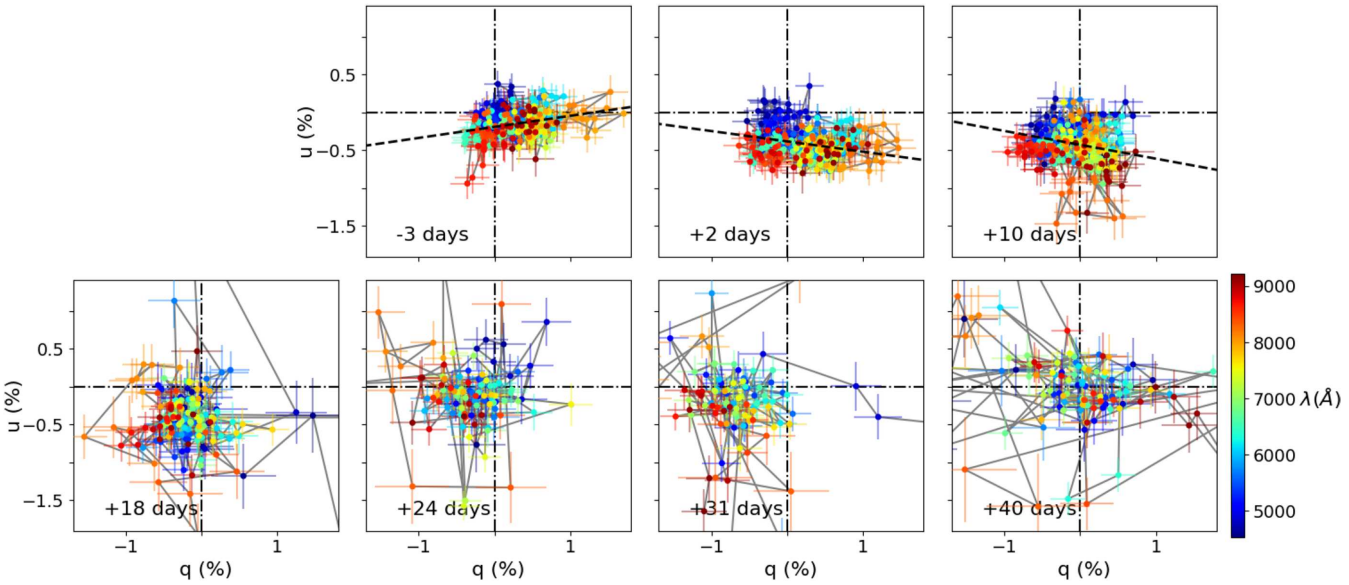

Figure 9. Stokes $q - u$ planes of the ISP corrected data of SN 2011hs from −3 to 40 d after V-band maximum. The data were binned to 15 Å and the colour scale represents wavelength. The dominant axes of epochs 1–3 are shown as the dashed black line, and were calculated using ODR.

is solely due to partial blocking of the photosphere by a non-isotropic distribution of the line-forming regions – our case (ii) described above – the observed values in P.A. would indicate that the asymmetries in these line-forming regions must individually follow a similar direction to the global asymmetry. On the other hand, a scenario in which the line polarization is the result of global geometry effects requires no serendipitous alignment, and we therefore prefer this interpretation.

In order to see a rotation in P.A. over time, a tri-axial geometry is required. A possible configuration could be an off-axis energy source within initially ellipsoidal ejecta. In the framework presented above, this would be a mixture of cases (iii) and (i). As the photosphere recedes through the ejecta, the off-axis energy source would be revealed and add a third axis to the original bi-axial geometry, causing a change in P.A. over time. Our estimates of the photospheric velocities (see Table 2) show that at the first two epochs the photosphere is found at −9860 and −8760 km s^{-1}, respectively. At epoch 3, when the rotation of the P.A. becomes significant, the photosphere has receded considerably down to −6320 km s^{-1}, which could have started to reveal a deeper off-centre energy source.

As previously mentioned, the emergence of an off-axis energy source at +10 d, breaking the initial bi-axial symmetry of the ejecta, would result in the loops on the $q - u$ plane. Indeed, we see that the calcium feature forms clear lines on the $q - u$ plots at −3 and +2 d, and then exhibits a clear loop at +10 d (see Fig. 10). This, however, is not seen in hydrogen or helium, which show loops at earlier dates. As described in Section 4.2, Hα has the clearest loop at −3 d, where hydrogen dominates the spectrum. The clarity of this loop diminishes over the next two epochs, whereas the He I λ5876 loop (non-existent at −3 d), becomes more distinct as helium starts dominating the spectrum. This seems to suggest that in addition to the global geometry effects dominating the P.A. behaviour of the line polarization features, there could be line specific effects. Therefore, some anisotropies in the distribution of the line-forming regions of hydrogen and helium – case (ii) – may also be present.

We want to emphasize that the possible solutions detailed in this section are non-unique. Additionally, they do not explain all of the observational characteristics described in Section 4. The drastic rotation of the P.A. of He I λ5876 at +18 d, which differs from the rotation of the continuum and other elements, remains unexplained. The cause for increase in polarization and rotation of the P.A. by ∼60° in the calcium data at later times is also unclear. Careful modelling is required, but is beyond the scope of this study.

5.2 Comparison to previous studies

As previously mentioned, Type IIb SNe are relatively well represented in the spectropolarimetry literature and a variety of spectropolarimetric evolutions have been observed for different objects. SN 2001ig only showed 0.2 per cent continuum polarization at early times, which then rose to ∼1 per cent after maximum light (Maund et al. 2007b). Other cases, exhibited strong continuum polarization early on, with Chornock et al. (2011) recording 0.64 per cent continuum polarization in SN 2008ax 9 d after explosion, or 12 d before V-band maximum. Stevance et al. (2016) also found significant continuum polarization (∼0.7 per cent) in SN 2008aq 16 d after explosion, or 4 d before V-band maximum. Subsequently, the continuum polarization of SN 2008aq rose above 1.2 per cent a week after maximum, therefore following a similar pattern to SN 2001ig.

The increase in polarization as the photosphere probes the deeper ejecta is not universal. Indeed SN 2011dh (Mauerhan et al. 2015) showed significant continuum polarization (0.45 per cent) at 9 and 14 d after explosion (i.e. 11 and 6 d before V-band maximum) and decreased to $p < 0.2$ per cent by 30 d after explosion (i.e. a week after V-band maximum). A similar behaviour is observed in SN 2011hs, where significant polarization $p = 0.55 \pm 0.12$ and 0.75 ± 0.11 per cent was seen at −3 and +2 d with respect to V-band maximum, and then decreased by ∼0.25 per cent by +10 d, down to ∼0.3 per cent at +18 d.

Another common feature of the SN 2011hs and SN 2011dh data is the coupling between the P.A. of the Hα and He I polarization and that of the continuum. Mauerhan et al. (2015) suggested this was best explained by clumpy excitation by plumes of nickel rising from the core. This could also be the case in SN 2011hs, and would fit in with the scenario of an off-axis energy source described in

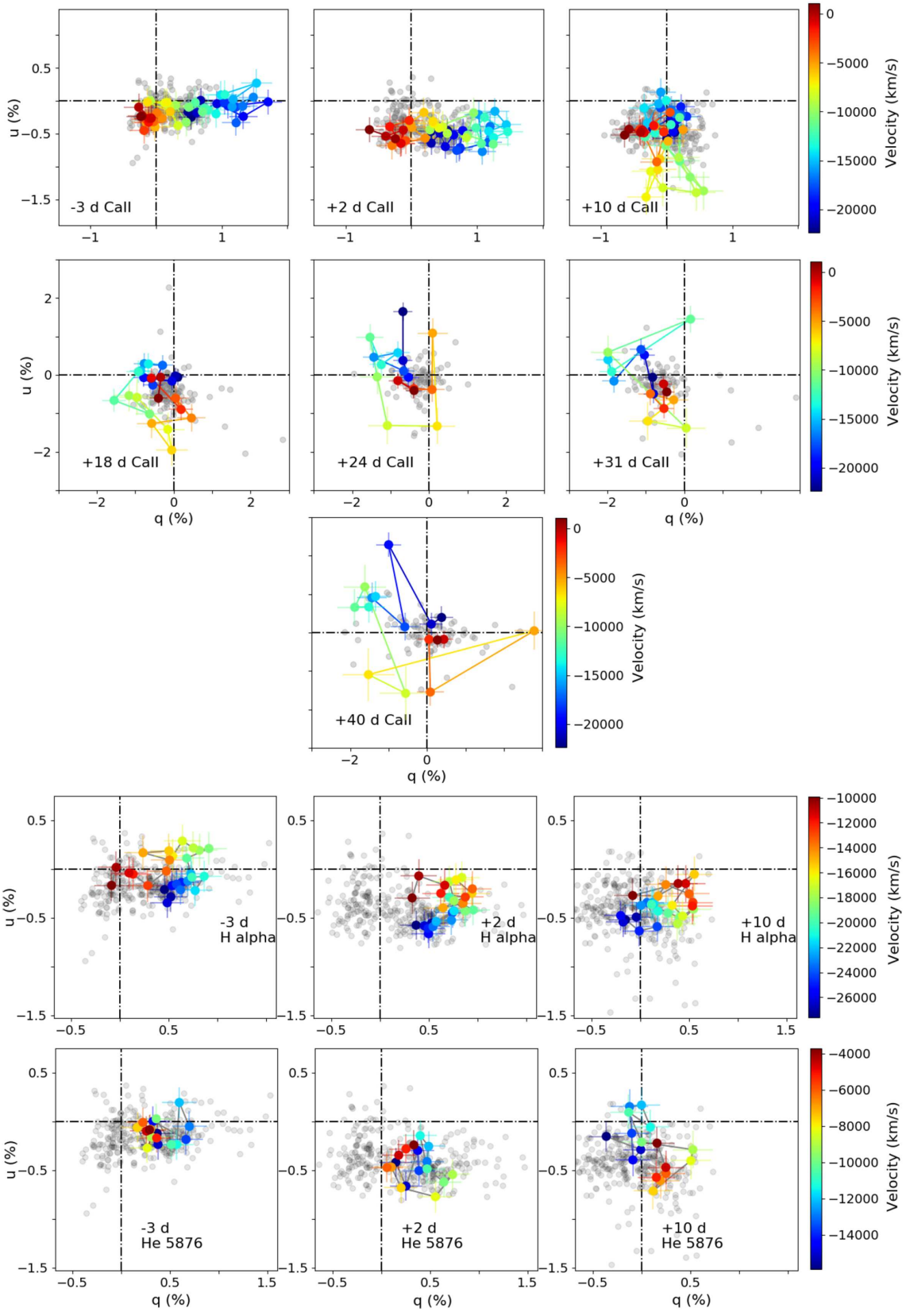

Figure 10. Stokes $q - u$ plots of the ISP corrected data of He λ5876 and Hα and Ca II. The colour scales represent velocity in km s^{-1} and vary between species for better visualization. The grey points show the rest of the data across the whole wavelength range covered by our observations.

Section 5.1, where ^{56}Ni plumes rising from the core could break the global bi-axial geometry of the outer ejecta.

The presence of an asymmetric nickel distribution could be due to numerous reasons. In the case of the jet powered bipolar explosion of SN 1987A, asymmetric nickel distribution was suggested to cause polarization (Chugai 1992). Alternatively, 3D simulations by Wongwathanarat, Janka & Müller (2013) showed asymmetric distributions of nickel in neutron star kick scenarios, where the iron group elements are ejected in the direction opposite that of the kick imparted on the remnant. These simulations, however, used progenitors of mass 15–20M$_\odot$ at explosion, which is not consistent with the mass limits derived by Bufano et al. (2014) for SN 2011hs ($M_{\rm ZAMS}$= 12-15M$_\odot$). This relatively low mass for the progenitor of SN 2011hs could imply the presence of a binary companion. Indeed, SN progenitors with $M_{\rm ZAMS} < 20\,{\rm M}_\odot$ require binary interaction to lose enough mass to result in stripped envelope SNe (Dessart et al. 2011). It was proposed by Höflich (1995) for the case of SN 1993J that an off-centre energy source could be the result of binary interaction, where the asymmetry results from the inner region of the ejecta still being accelerated by the gravitational potential of the binary whereas the faster outer regions are driven far from the orbit of the system very early. Furthermore, the binary scenario could also explain the early asphericity through binary interaction, similarly to the case of SN 2001ig (Maund et al. 2007b). Note, however, that this is a non-unique solution to our data.

Certainly one of the most shared characteristics of Type IIb SNe is the presence of line polarization associated with He I λ5876 and Hα. In Fig. 11, we place SN 2011hs in the context of other SNe at similar spectral stages (where hydrogen dominates and where helium starts becoming prominent). We would like to emphasize that the spectropolarimetric behaviour of Type IIb SNe is non-uniform. Some SNe (SN 2008aq and SN 2011dh) show a strong blend of the helium and hydrogen polarization features before helium features start strengthening as the photosphere recedes through the ejecta. At later dates, once helium lines become stronger, the Hα feature separates from the He I λ5876 and two distinct peaks are visible. In other cases, e.g. SN 2008ax and SN 2011hs, two distinct peaks of Hα and He I λ5876 can be seen even before helium spectral features start deepening. It is interesting that SN 2011hs and SN 2011dh behave differently in this respect, despite the other commonalities in their spectropolarimetric characteristics. These disparities should be reproduced by future models of the spectropolarimetry of Type IIb SNe.

The presence of loops associated with the polarization of strong lines has also been observed repeatedly in Type IIb SNe. One of the most extreme cases was Hα in SN 2008ax (Chornock et al. 2011 see their figs 13 and 14). In SN 2011hs, we saw loops of Hα and He I λ5876 at early times. Hydrogen exhibited the most prominent loop at −3 d when hydrogen was strongest in the spectrum, whereas the helium loop only arose at +2 d and grew at +10 d as the helium lines strengthened. In SN 2011dh, the best defined hydrogen loops are also found before helium starts showing prominent features in the flux spectrum (see fig. 4 of Mauerhan et al. 2015). Contrary to SN 2011hs, however, SN 2011dh shows significant loops in He I λ5876 even at the earliest times. Another major difference between these two objects is in their calcium loops. As we saw in Section 4.2, the calcium data in SN 2011hs have a linear structure on the $q - u$ plane around maximum light, and only starts exhibiting a loop 10 d after V-band maximum. In contrast, SN 2011dh shows its strongest calcium loop at the earliest epoch (9 d after explosion or 11 d before V-band maximum).

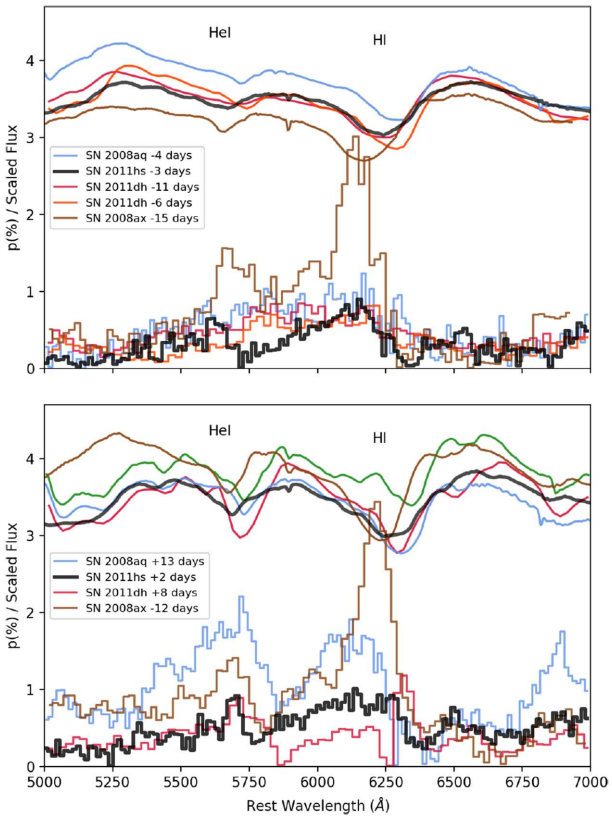

Figure 11. Hα and He I λ5876 polarization features in phases where hydrogen dominates (top panel) and after helium has strengthened (bottom panel). We show SN 2011hs, SN 2008ax (Chornock et al. 2011), SN 2011dh (Mauerhan et al. 2015), and SN 2008aq (Stevance et al. 2016). The polarization data are shown as step plots and the flux spectra are plotted for comparison as smooth curves. Note that the phases are quoted with respect to V-band maximum instead of explosion date.

These differences in the loop behaviour of Type IIb SNe, and the precise origin of the loops of Hα and He Iλ5876 in SN 2011hs at the first two epochs, are difficult to understand without modelling. Toy models have been used in the past (e.g. Maund et al. 2010, Reilly et al. 2016), to try to reproduce line polarization and constrain the ejecta geometry. In an attempt to understand the early hydrogen and helium loops (and potentially extend this to other SNe), we created a model based on the same assumptions, but used a more methodical approach to explore parameter space (Stevance, in preparation). The result of this work, however, was to demonstrate the great number of degeneracies that arise in such models even when considering a small number of free parameters, as well as the fact that it can result in good fits to the data even in cases were the original assumptions are invalid. This highlights the fact that simplified models must be considered very carefully as they may yield misleading results.

Full hydrodynamic simulations with radiative transfer that can simultaneously reproduce the flux spectrum and the corresponding polarization features will be necessary to better understand the varied geometry of Type IIb and other CCSNe. Additionally, higher cadence observations, especially around and soon after maximum light, could help better understand the variations of the ejecta geometry with depth.

6 CONCLUSIONS

We presented seven epochs of spectropolarimetry for the Type IIb SN 2011hs from −3 to +40 d with respect to *V*-band maximum. The observed polarimetry data showed very high levels of polarization increasing towards blue wavelengths (up to ∼3 per cent). We quantified the ISP and identified that most of the observed polarization was caused by the interstellar component. Fits of the Serkowski law (Serkowski et al. 1975) allowed us to constrain λ_{max} to wavelengths < 4245 Å or < 4700 Å, depending on the value of K used, either from Serkowski et al. (1975) or Whittet et al. (1992), respectively. Such levels of ISP have never been observed in a Type IIb SN before. Similar behaviours of the interstellar component, with low values of λ_{max}, have been seen in some Type Ia SNe (Patat et al. 2015). This may suggest enhanced levels of small silicate grains, either resulting from cloud–cloud collisions caused by SN radiation pressure, or due to the destruction of large grains by the radiation field (Hoang 2017; Hoang et al. 2018). Consequently, the behaviour and level of the ISP in the spectropolarimetric data of SN 2011hs seem to indicate the presence of dust in the vicinity of the SN, which could reflect the mass-loss history of the progenitor.

The intrinsic polarization of SN 2011hs was retrieved after removal of the ISP component. Significant continuum polarization was observed at the first two epochs, with $p = 0.55 \pm 0.12$ per cent and 0.75 ± 0.11 per cent, respectively, corresponding to ∼10 per cent departure from spherical geometry, in the context of an oblate spheroid (Höflich 1991). The continuum polarization then decreased by ∼0.25 per cent by +10 d and declined further by +18 d. A strong correlation was found between the behaviour of the P.A. of hydrogen, helium, calcium, and that of the continuum, indicating they share a common geometry. The progressive rotation of the continuum P.A. after epoch 2 can be interpreted as the presence of an off-centre energy source being revealed. This is supported by the calcium data on the $q - u$ plane, where a dichotomy exists between the first two epochs at which the data form a line (indicating bi-axial geometry), and the following epochs at which loops are observed (evidence for a departure from bi-axial geometry).

On the other hand, Hα shows the clearest loop at the first epoch when hydrogen is strongest in the spectrum. It then diminished as He Iλ5876 starts to show a loop by +3 d, which strengthens by +10 d, where helium is starting to dominate the spectrum. These characteristics show that the lines of hydrogen and helium probe tri-axial geometries at early times where calcium does not, and therefore line specific geometries must also be a contributor to their polarization. A possibility would be the presence of anisotropies in the distribution of their line-forming regions.

Compared to previously studied Type IIb SNe, SN 2011hs is most similar to SN 2011dh (Mauerhan et al. 2015), where a decrease in continuum polarization over time and a correlation between the P.A. of hydrogen, helium, and the continuum was observed. Mauerhan et al. also favoured an off-centre source of energy to explain their observations, namely in the form of plumes of nickel. This could also be consistent with SN 2011hs, but is not unique and is probably an insufficient solution to our observations.

Lastly, there are a number of features whose origins remain unknown. At +18 d, the P.A. of He Iλ5876 undergoes a drastic rotation that is not coupled with that of the continuum or other elements. Additionally, the calcium data at later dates see an increase in polarization and a rotation in P.A. by $+60^{\circ}$.

On the whole, SN 2011hs brings to our sample of Type IIb SN spectropolarimetry data a number of features that have been previously seen as well as new disparities that need to be explained. It is clear from examples such as SN 1993J, SN 2001ig, SN 2008aq, SN 2008ax, SN 2011dh, and SN 2011hs that there is great variety in the observed spectropolarimetric, and therefore geometric, properties of Type IIb SNe (Tran et al. 1997; Höflich 1995; Maund et al. 2007b; Stevance et al. 2016; Chornock et al. 2011; Mauerhan et al. 2015). More observations, especially with a higher cadence around and after maximum, and detailed hydrodynamic models with radiative transfer of the current and future spectropolarimetric data are required for us to better understand the similarities and the diversity in the geometries of Type IIb SNe.

ACKNOWLEDGEMENTS

The authors would like to thank the staff of the Paranal Observatory for their kind support and for the acquisition of such high-quality data on the program 088.D-0761. This work has made use of data from the European Space Agency mission *Gaia* (https://www.cosmos.esa.int/gaia), processed by the *Gaia* Data Processing and Analysis Consortium (DPAC, https://www.cosmos.esa.int/web/gaia/dpac/consortium). Funding for the DPAC has been provided by national institutions, in particular the institutions participating in the Gaia Multilateral Agreement. We are grateful to S. Parsons for sharing his expertise on white dwarf flux calibration, S. Couch for bringing an insightful reference to our attention, and L. Grimmett for our numerous discussions concerning statistics. HFS and JB are supported through a PhD scholarship granted by the University of Sheffield. JCW is supported by the Samuel T. and Fern Yanagisawa Regents Professorship in Astronomy and by NSF Grant 1813825. AC is supported by grant IC120009 (MAS) funded by the Chilean Ministry of Economy, Development, and Tourism, and by grant Basal CATA PFB 06/09 from CONICYT. The research of JRM is supported through a Royal Society University Research Fellowship. The following packages were used for the data reduction and analysis: MATPLOTLIB (Hunter 2007), ASTROPY (The Astropy Collaboration et al. 2018), NUMPY, SCIPY, and PANDAS (Jones et al. 2017).

REFERENCES

Anderson C. M. et al., 1996, AJ, 112, 2726
Appenzeller I. et al., 1998, The Messenger, 94, 1
Branch D., Wheeler J. C., 2017, Supernova Explosions. Springer-Verlag GmbH, Germany
Bufano F. et al., 2014, MNRAS, 439, 1807
Burrows A., 2013, Rev. Mod. Phys., 85, 245
Chandrasekhar S., 1946, ApJ, 103, 351
Chornock R. et al., 2011, ApJ, 739, 41
Chugai N. N., 1992, SvA Lett., 18, 168
Cikota A., Patat F., Cikota S., Spyromilio J., Rau G., 2017, MNRAS, 471, 2111
Dessart L., Hillier D. J., Livne E., Yoon S.-C., Woosley S., Waldman R., Langer N., 2011, MNRAS, 414, 2985
Eldridge J. J., Fraser M., Smartt S. J., Maund J. R., Crockett R. M., 2013, MNRAS, 436, 774
Filippenko A. V., 1997, ARA&A, 35, 309
Fox O. D. et al., 2014, ApJ, 790, 17
Heiles C., 2000, AJ, 119, 923
Hoang T., 2017, ApJ, 836, 13
Hoang T., Tram L. N., Lee H., Ahn S.-H., 2018, preprint (arXiv:1810.05557)
Höflich P., 1991, A&A, 246, 481
Höflich P., 1995, ApJ, 440, 821
Höflich P., Wheeler J. C., Wang L., 1999, ApJ, 521, 179

Ho L. C., Li Z.-Y., Barth A. J., Seigar M. S., Peng C. Y., 2011, ApJS, 197, 21
Hunter J. D., 2007, Comput. Sci. Eng., 9, 90
Janka H.-T., 2012, Annu. Rev. Nucl. Part. Sci., 62, 407
Jones E. et al., 2017, SciPy: Open Source Scientific Tools for Python., Available at: http://www.scipy.org/. Last accessed date 31st of January
Kasen D. et al., 2003, ApJ, 593, 788
Koribalski B. S. et al., 2004, AJ, 128, 16
Leonard D. C. et al., 2006, Nature, 440, 505
Luri X. et al., 2018, A&A, 616, A9
Martin P. G., Clayton G. C., Wolff M. J., 1999, ApJ, 510, 905
Mauerhan J. C. et al., 2015, MNRAS, 453, 4467
Maund J. R. et al., 2010, ApJ, 722, 1162
Maund J. R., 2008, A&A, 481, 913
Maund J. R., Smartt S. J., Kudritzki R. P., Podsiadlowski P., Gilmore G. F., 2004, Nature, 427, 129
Maund J. R., Wheeler J. C., Patat F., Baade D., Wang L., Höflich P., 2007a, MNRAS, 381, 201
Maund J. R., Wheeler J. C., Patat F., Wang L., Baade D., Höflich P. A., 2007b, ApJ, 671, 1944
Maund J. R., Wheeler J. C., Baade D., Patat F., Höflich P., Wang L., Clocchiatti A., 2009, ApJ, 705, 1139
McCall M. L., 1984, MNRAS, 210, 829
Milisavljevic D., Fesen R., Soderberg A., Pickering T., Kotze P., 2011, CBET, 2902, 2
Patat F. et al., 2015, A&A, 577, A53
Poznanski D., Prochaska J. X., Bloom J. S., 2012, MNRAS, 426, 1465
Reilly E. et al., 2016, MNRAS, 457, 288
Schlafly E. F., Finkbeiner D. P., 2011, ApJ, 737, 103
Serkowski K., 1973, in Greenberg J. M., van de Hulst H. C., eds, IAU Symp. Vol. 52, Interstellar Dust and Related Topics. Kluwer, Dordrecht, p. 145
Serkowski K., Mathewson D. S., Ford V. L., 1975, ApJ, 196, 261
Shapiro P. R., Sutherland P. G., 1982, ApJ, 263, 902
Silverman J. M., Mazzali P., Chornock R., Filippenko A. V., Clocchiatti A., Phillips M. M., Ganeshalingam M., Foley R. J., 2009, PASP, 121, 689
Smartt S. J., 2009, ARA&A, 47, 63
Smith N., Li W., Filippenko A. V., Chornock R., 2011, MNRAS, 412, 1522
Stevance H. F. et al., 2016, MNRAS, 461, 2019
Stevance H. F. et al., 2017, MNRAS, 469, 1897
Stevance H. F., Ignace R., Crowther P. A., Maund J. R., Davies B., Rate G., 2018, MNRAS, 479, 4535
Tanaka M., Maeda K., Mazzali P. A., Kawabata K. S., Nomoto K., 2017, ApJ, 837, 105
The Astropy Collaboration et al., 2018, AJ, 156, 123
Trammell S. R., Hines D. C., Wheeler J. C., 1993, ApJ, 414, L21
Tran H. D., Filippenko A. V., Schmidt G. D., Bjorkman K. S., Jannuzi B. T., Smith P. S., 1997, PASP, 109, 489
van de Hulst H. C., 1957, Light Scattering by Small Particles. John Wiley & Sons, New York
Wang L., Wheeler J. C., 1996, ApJ, 462, L27
Wang L., Wheeler J. C., 2008, ARA&A, 46, 433
Wang L., Howell D. A., Höflich P., Wheeler J. C., 2001, ApJ, 550, 1030
Whittet D. C. B., Martin P. G., Hough J. H., Rouse M. F., Bailey J. A., Axon D. J., 1992, ApJ, 386, 562
Wongwathanarat A., Janka H.-T., Müller E., 2013, A&A, 552, A126

This paper has been typeset from a TEX/LATEX file prepared by the author.